Journal of Physics: Complexity

PAPER • OPEN ACCESS

Atlas of urban scaling laws

To cite this article: Anna Carbone *et al* 2022 *J. Phys. Complex.* **3** 025007

Journal of Physics: Complexity

OPEN ACCESS

RECEIVED
4 October 2021

REVISED
8 April 2022

ACCEPTED FOR PUBLICATION
19 May 2022

PUBLISHED
6 June 2022

PAPER

Atlas of urban scaling laws

Anna Carbone[1,*], Pietro Murialdo[1], Alessandra Pieroni[2] and Carina Toxqui-Quitl[3]

[1] Politecnico di Torino, Italy
[2] Agenzia per l'Italia Digitale, Roma, Italy
[3] Universidad Politécnica de Tulancingo, Hidalgo, Mexico
[*] Author to whom any correspondence should be addressed.

E-mail: anna.carbone@polito.it

Keywords: detrending moving average algorithm, urban scaling laws, heterogeneous fractal systems

Abstract

Accurate estimates of the urban fractal dimension D_f are obtained by implementing the detrended moving average algorithm on high-resolution multi-spectral satellite images from the WorldView2 (WV2) database covering the largest European cities. Fractal dimension D_f varies between 1.65 and 1.90 with high values for highly urbanised urban sectors and low ones for suburban and peripheral ones. Based on recently proposed models, the values of the fractal dimension D_f are checked against the exponents β_s and β_i of the scaling law $Y \sim N^{\beta}$, respectively for socio-economic and infrastructural variables Y, with N the population size. The exponents β_s and β_i are traditionally derived as if cities were zero-dimensional objects, with the relevant feature Y related to a single homogeneous population value N, thus neglecting the microscopic heterogeneity of the urban structure. Our findings go beyond this limit. High sensitive and repeatable satellite records yield robust local estimates of the urban scaling exponents. Furthermore, the work discusses how to discriminate among different scaling theories, shedding light on the debated issue of scaling phenomena contradictory perspectives and pave paths to a more systematic adoption of the complex system science methods to urban landscape analysis.

1. Introduction

The idea of quantifying socio-economic phenomena in terms of laws derived from statistical physics and complex systems science continues to spread as more and more accurate time and space dependent data become available. Hence, early studies evidencing that diverse socio-economic processes obey certain empirical laws can be supported by robust statistical modelling [1, 2]. Despite the diversity of historical and geographical contexts, several urban features Y have been linked to the population size N by power-laws $Y \sim N^{\beta}$. Socio-economic features (e.g. patent production, gross domestic product, crime, pollution) tend to scale super-linearly, with $\beta > 1$. On the other hand, physical infrastructure features (e.g. transportation, financial services) tend to increase sub-linearly, with $\beta < 1$. Individual needs (e.g. housing, water consumption) tend to scale linearly with $\beta \approx 1$ [3]. Diverse theories, e.g. based on dissipative interactions [4], gravity [5], three-dimensional fractal buildings [6], self-organization [7] and synergetics [8], have been proposed to describe the microscopic origin of such behaviour. A feature common to these models is that the interactions depend on the effective distance ℓ connecting site pairs, which for fractal media, is expressed in terms of the Hausdorff dimension as $\ell \propto \lambda^{D_f}$ (figure 1). Then the fractal (Hausdorff) dimension D_f is linked to the exponent β, hence bridging together the urban scaling and fractal geometry research areas and opening novel directions to the quantitative analysis of socio-economic phenomena and urban complex systems.

Morphology and function of cities are prominent examples of fractals with the Hausdorff dimension D_f providing a measure of the urban concentration across scales [9, 10]. The estimation of fractal dimension in urban contexts begins by analysing the spatial distribution of the build-up area, traditionally performed on cartographic images with black pixels corresponding to built-up space and resolution defined by the size of the pixels. While a uniform distribution of buildings over the investigated area would yield a fractal dimension D_f

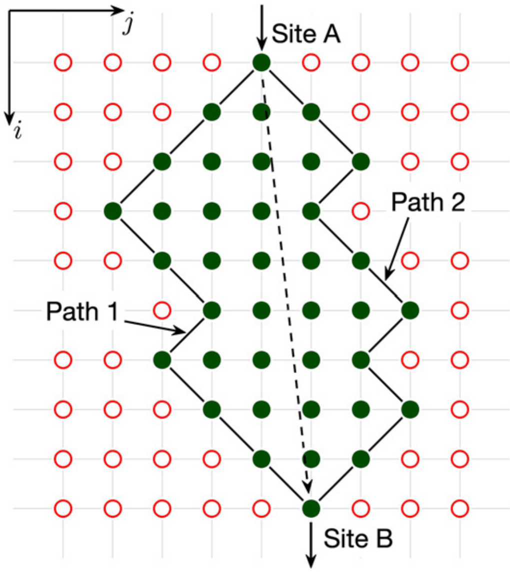

Figure 1. Individual path samples between urban site pairs A and B with characteristic length ℓ. Two paths connecting a pair of sites, define the boundary of a urban cluster with area A. The length ℓ can be related to the average size (diameter) of the area $\lambda = A^{1/d}$ and to the fractal dimension D_f by the relationship $\ell \propto \lambda^{D_f} = A^{D_f/d}$.

almost equal to the Euclidean dimension d ($D_f \sim d$), a sparse distribution of buildings provides values lower than d ($D_f < d$) [11].

Urban infrastructures cannot be simply quantified by iteration of elementary constituents, as it would be appropriate for deterministic fractals. Statistically based elaboration of data mapped on the coordinates i, j of the city grid are required. Methods as diverse as radial and box counting, isarithm, triangular prism, and variogram have been adopted [10–20].

Despite extensive efforts and several successful applications [21–26], many issues are still unsolved preventing full acceptance of the urban scaling ideas [27–30]. Concerns refer for example to the microscopic origin of the scaling behaviour, to the analytical relationships linking the exponents β and D_f, to the accuracy of statistical fitting. Different outcomes have been obtained even for the same city due to computing-method variations, disparities in map size, coverage and boundary, resolution, data accuracy, time period, box-size and scale. The scaling exponent β and the fractal dimension D_f heavily depend on the definitions, methods and variables chosen for their estimation, varying significantly among different works and irremediably defying the intended universality. Dataset heterogeneity and incompleteness represent a severe limitation to the accuracy and ultimately prevent the comparison of the scaling exponents across different cities. Digitally collected data have the potential to provide objective features and comparable estimates across different regions. In particular, satellite technologies, yielding regularly and uniformly recorded data with well-defined features, are conveniently exploited to gather information about infrastructural and socio-economic features [31–36]. However, the ever increasing variety and volume of data pose additional constraints to their practical usability, requiring more and more sophisticated computational tools.

It is noteworthy that most of the empirical estimates of the scaling exponents made in the literature use socio-economic quantities of employment or added values, which are not provided by a pointwise distribution over the urban areas and certainly they are not detectable, nor can be provided by satellite images, which refer to physical information of rural and urban landscapes. Models like those proposed in [4–8] might be very relevant to overcome this limitation, as they share the common aim to relate the physical/infrastructural features to the socio-economic variables. Further scientific steps are still required in order to shed light on the physical hypothesis and mathematical constraints underlying the existing literature in order to find a unified view of the described phenomena and remove all the apparent contradictions still present in the outcomes fueling controversial perspectives.

This work addresses some of the above challenges. Firstly, robust estimates of the fractal dimensions D_f of urban and suburban sectors are obtained by implementing the two-dimensional *detrended moving average* (DMA) [39] on 1.84 m-resolution WorldView-2 satellite images of several cities [40]. For centrally located urban areas characterized, by regular building grid, fractal dimension values close to 1.9 are found. Suburban and peripheral areas are characterised by lower fractal dimension with values close to 1.6. Secondly, the dependence of the exponents β on the fractal dimension D_f is discussed on account of the empirical values for socio-economic and infrastructural quantities reported in [3] and the behaviour expected on account of the models [4–6]. By taking advantage of the accuracy of the DMA method and high resolution repeatable satellite records, the proposed approach yields statistically robust estimates of the scaling exponents for urban and suburban sectors. It is worthnoting that central and peripheral parts of European urban agglomerations have been discriminated by means of alternative approaches based on radial distribution density $D(r)$ and cumulative population function $P(r)$ of the CORINE Land Cover database images [17] and of the Urban Atlas database [18].

The manuscript is organized as follows. In section 2 (definitions and methods) the fractal dimension, the fractional Brownian field and the DMA method are briefly recalled. In section 3 (data and results) the World-View2 satellite images are described and a few examples are shown (Turin, Wien, Zurich, Prague). The fractal dimensions D_f are estimated for different urban and suburban sectors of the same city. In section 4 (discussion), comparison with previously published results and validation against urban scaling models, in terms of the β vs D_f relationships, are provided. In section 5 (conclusion) the main outcomes, potential implications and directions for future work are summarised.

2. Definitions and methods

Self-similarity concepts and fractal geometry have been extensively adopted to describe real-world structures characterized by irregular fragmented shapes and complex features that traditional approaches fail to grasp. Scaling relations of the form:

$$f(\lambda) \propto \lambda^{D_f}, \tag{1}$$

are generally exhibited by self-similar textures where λ is a characteristic scale, a measuring unit size, and D_f the fractal (Hausdorff) dimension, defined as:

$$D_f = d - H, \tag{2}$$

with d the Euclidean embedding dimension and H the Hurst exponent, ranging from $0 < H < 0.5$ and $0.5 < H < 1$, respectively for negatively and positively correlated random sets, and $H = 0.5$ corresponding to the ordinary Brownian function, i.e. to fully uncorrelated random sets.

Fractional Brownian fields, i.e. continuous functions of two variables $f_H(x_1, x_2)$ can be conveniently adopted for spatial data modelling [37, 38]. The Hurst exponent H characterizes the degree of irregularity which decreases as H increases. The Hurst exponent uniquely characterizes the fractional Brownian field and can be used in equation (2) to estimate the fractal dimension D_f, which instead is not uniquely defined and depends on d. The fractal dimension D_f of the fractional Brownian surface is $D_f = 2 - H$ when referred to an horizontal cross section of the fractal set (i.e. a curve with dimension varying between a line 1 and a plan 2), whereas for the whole fractal set, i.e. a geometric structure varying between a plan and a volume, $D_f = 3 - H$ [37]. Since the value of the fractal dimension D_f depends on the topological dimension d, it is convenient to take the Hurst exponent as a metric of the random field, whereas D_f might be useful to graphically envision the irregular structure. Several realizations of the fractional Brownian random fields for different values of the Hurst exponent H have been graphically represented with $d = 2$ in [39] and with $d = 3$ in [42, 43].

As mentioned in the introduction, the high-dimensional DMA (d-DMA) [39] is here applied to World-View2 satellite images [40] to estimate the Hurst exponent H and fractal dimension D_f of urban infrastructures. For the sake of clarity, the main steps of the DMA method are briefly summarized below.

Random fractal sets can be analytically described in terms of a scalar function $f_H(r) : \mathbb{R}^d \to \mathbb{R}$ showing self-similarity, with the Hurst exponent H as a parameter, and correlation function:

$$C_H(r, r + \lambda) = \frac{\sigma^2}{2}\left[|\lambda|^{2H} + |r + \lambda|^{2H} - |r|^{2H}\right] \tag{3}$$

depending as a power law on the scale λ and $H \in [0, 1]$. The power-law correlation is reflected by the variance:

$$\sigma_H^2 = \left\langle [f_H(r + \lambda) - f_H(r)]^2 \right\rangle \propto \|\lambda\|^{2H} \tag{4}$$

with $r = (x_1, x_2, \ldots, x_d)$, $\lambda = (\lambda_1, \lambda_2, \ldots, \lambda_d)$ and $\|\lambda\| = (\lambda_1^2 + \lambda_2^2 + \cdots + \lambda_d^2)^{1/2}$.

As schematically illustrated in figure 2, the DMA algorithm operates via a generalized high-dimensional variance σ_{DMA} of $f_H(r)$ around the moving average function $\tilde{f}_H(r)$ [39], that, for $d = 2$, writes:

$$\sigma_{DMA}^2 = \frac{1}{(N_1 - n_{1_{max}})(N_2 - n_{2_{max}})} \times \sum_{i_1=n_1}^{N_1} \sum_{i_2=n_2}^{N_2} [f(i_1, i_2) - \tilde{f}_{n_1 n_2}(i_1, i_2)]^2, \tag{5}$$

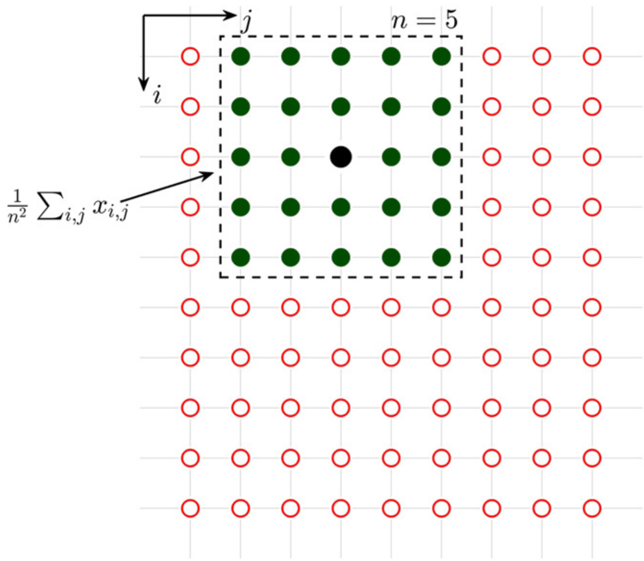

Figure 2. Scheme of the DMA algorithm operation on a two dimensional domain. Given a matrix M, for each moving average windows n_i and n_j, a matrix $\tilde{M}^{i,j}$, where each element $\tilde{M}^{i,j}$ is equal to the moving average window around M, is obtained. $\tilde{M}^{i,j}$ is then used to detrend $M^{i,j}$ according to the algorithm described in section 2.

with $\tilde{f}_{n_1 n_2}(i_1, i_2)$ given by:

$$\tilde{f}_{n_1 n_2}(i_1, i_2) = \frac{1}{n_1 n_2} \times \sum_{k_1=0}^{n_1-1} \sum_{k_2=0}^{n_2-1} f(i_1 - k_1, i_2 - k_2). \tag{6}$$

First, the average scalar field $\tilde{f}_{n_1 n_2}(i_1, i_2)$ is estimated over sub-arrays with different size $n_1 \times n_2$. The next step of the algorithm is the calculation of the difference $f(i_1, i_2) - \tilde{f}_{n_1,n_2}(i_1, i_2)$ for each sub-array $n_1 \times n_2$. It can be shown that equation (5) reduces to the form:

$$\sigma^2_{\mathrm{DMA}} \sim \left[\sqrt{n_1^2 + n_2^2}\right]^{2H} = s^H, \tag{7}$$

hence a log–log plot of σ^2_{DMA} as a function of $s = n_1^2 + n_2^2$ yields a straight line with slope H.

The scaling behaviour expected by equation (7) is illustrated in figure 3 where the $2d$-DMA method is implemented on artificial fractal images, with different size and Hurst exponent, generated by Cholesky–Levinson factorization [41]. One of such surfaces with $H = 0.2$ is shown in figure 3 (top panel). The σ_{DMA} values obtained for artificial fractal surfaces with input Hurst exponent ranging from 0.1 to 0.9, size 480×480 and 1024×1024 are plotted in the middle and bottom panels. The difference between the input Hurst exponents and the DMA outcomes is negligible and decreases as the size of the surface increases.

As opposed to fractional Brownian functions $f_{\mathrm{H}}(r)$ defined to exist at all scales, real-world data sets barely behave as ideal fractals. Being characterized by finite sizes, setting upper and lower limits to the detection of small and large scales, deviations from the ideal scaling behaviour should be expected.

Deviations at large scales are caused by finite-size effects, which occur when the analysed surfaces does not contain a sufficient amount of data to allow for a statistically significant evaluation of the scaling law for large values of the moving average window n. Finite-size effects become negligible for $n_{1,\max} \ll N_1$ and $n_{2,\max} \ll N_2$. On the other hand, deviations at small scales occur when the low-pass filter deviates from ideality. As discussed in [39] with respect to the *transfer function* $\mathcal{H}_{\mathcal{T}}(\omega_1, \omega_2)$ of the moving average low pass filter for $d = 2$, in ideal operations, $\mathcal{H}_{\mathcal{T}}$ should be one or zero respectively for frequencies lower or higher than the cutoff frequency. However, for real low-pass filters, at frequencies below the cutoff, signals suffer attenuation, while at frequencies over the cutoff, signals are not fully filtered out, causing $\mathcal{H}_{\mathcal{T}}$ to take values respectively smaller or larger than 1. This results in an excess of components with high frequency and a lack of components with low frequency, which in turn cause a decrease in the value of σ^2_{DMA} and therefore an increase of the slope in the log–log plot, resulting in deviations of the scaling law from the full linearity.

Equations (5)–(7) have been implemented on $d = 2$ and $d = 3$ artificially generated structures in [42, 43]. Multi-spectral LandSat Thematic Mapper imagery of rural areas of Mangystan (Kazakhstan) and New Mexico

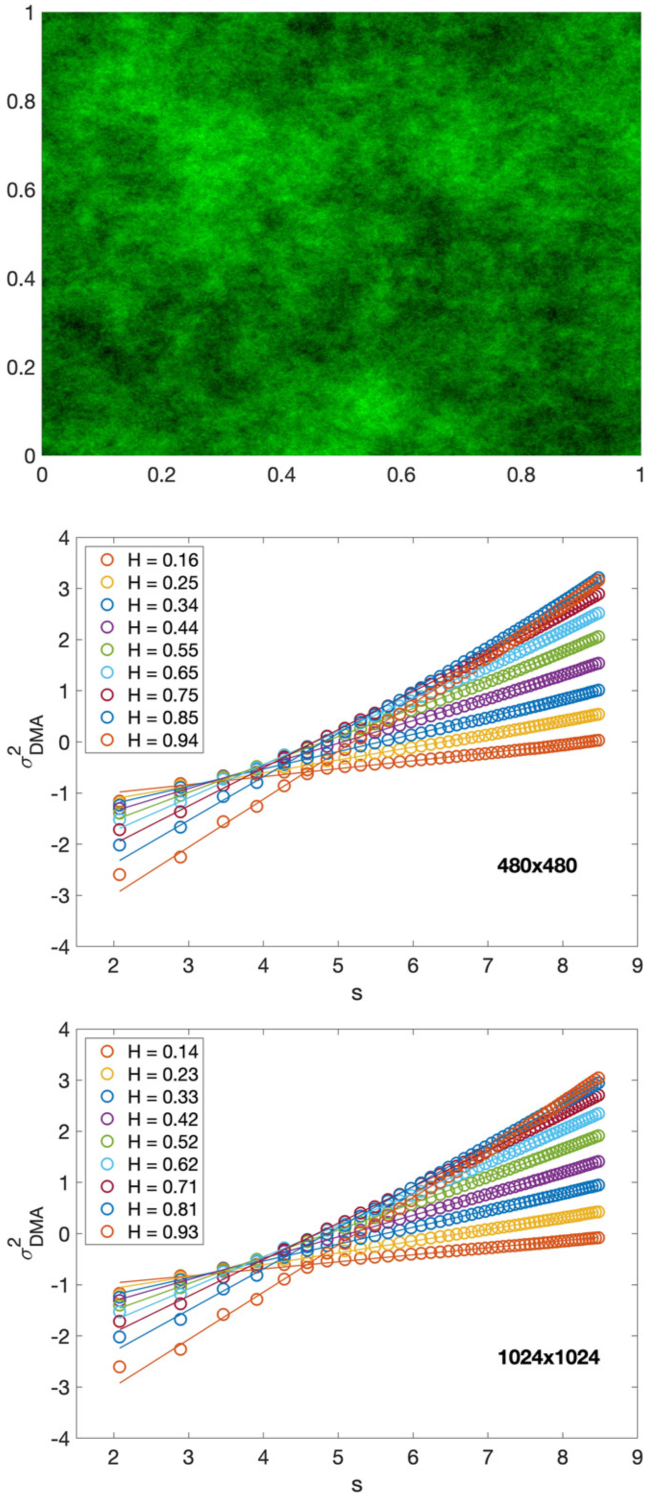

Figure 3. (Top panel) Fractional Brownian surface with size 512×512 and Hurst exponent $H = 0.2$ generated via FRACLAB [41]. (Middle panel) Log–log plots of σ^2_{DMA} results for fractional Brownian surfaces with Hurst exponent $H = 0.1, 0.2, 0.3, \ldots, 0.9$ and size 480×480. Log–log axis are in natural base. Each color refers to DMA results and to Hurst exponent estimates H for a different fractional Brownian surface. The Hurst exponent estimates reported in the legend are obtained as the slope of the regression line by least squares of log σ^2_{DMA}. (Bottom panel) Same as the middle panel but for surfaces with size 1024×1024.

(USA), monthly recorded from July 1982 to May 2012, have been analysed in [44]. Hurst exponents ranging between $0.21 \leqslant H \leqslant 0.30$ and $0.11 \leqslant H \leqslant 0.30$, corresponding to fractal dimensions between $1.70 \leqslant D_{\mathrm{f}} \leqslant 1.79$ and $1.70 \leqslant D_{\mathrm{f}} \leqslant 1.89$, have been found respectively for Mangystan and New Mexico. The increase of the fractal dimensions over the years has been interpreted in terms of the effect of the growth of man-made infrastructures and built-up areas at the expenses of the rural landscape.

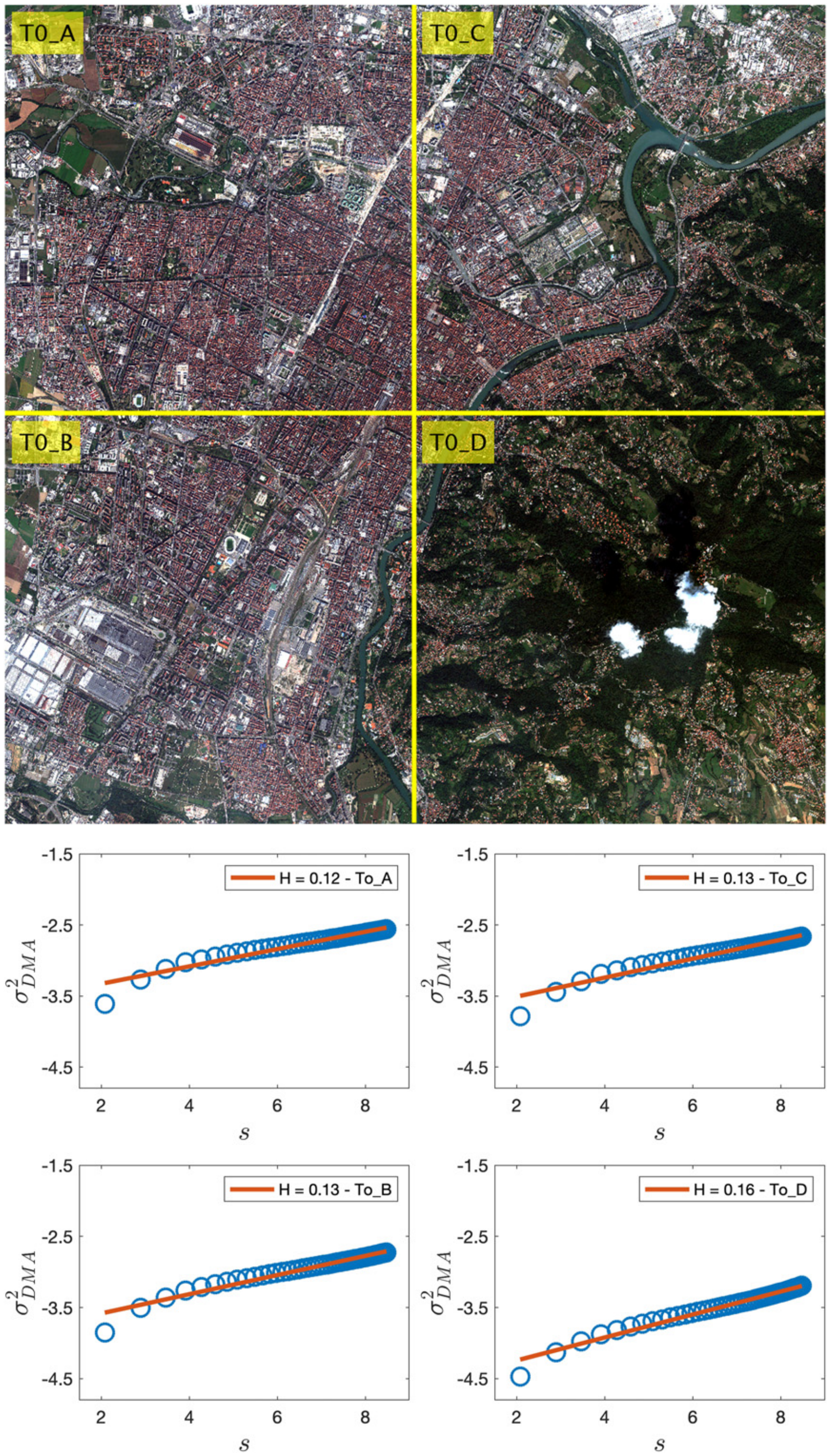

Figure 4. (Top panel) Image N45-024 (Torino) downloaded from the *Urban Atlas* collection of the largest European cities of WorldView-2 satellite images [40]. The image is multi-spectral with size 1080 × 1080. Yellow lines divide the image into four sub-images of size 540 × 540. (Bottom panel) Log–log plots of σ^2_{DMA} for each sub-image and for the red band. Log–log axis are in natural base. Hurst exponent estimates H, obtained as the slope of the regression line by least squares, are shown for each sub-image. Goodness of fit is evaluated by R^2 provided in table 1.

In this work, the Hurst exponent and the fractal dimension of WorldView2 satellite images of several cities will be estimated by using the two-dimensional detrending moving average algorithm (DMA) described by the equations (5)–(7) with the main purpose to investigate if the method can provide meaningful information regarding the variability of urban and suburban sectors within the same area and between different cities.

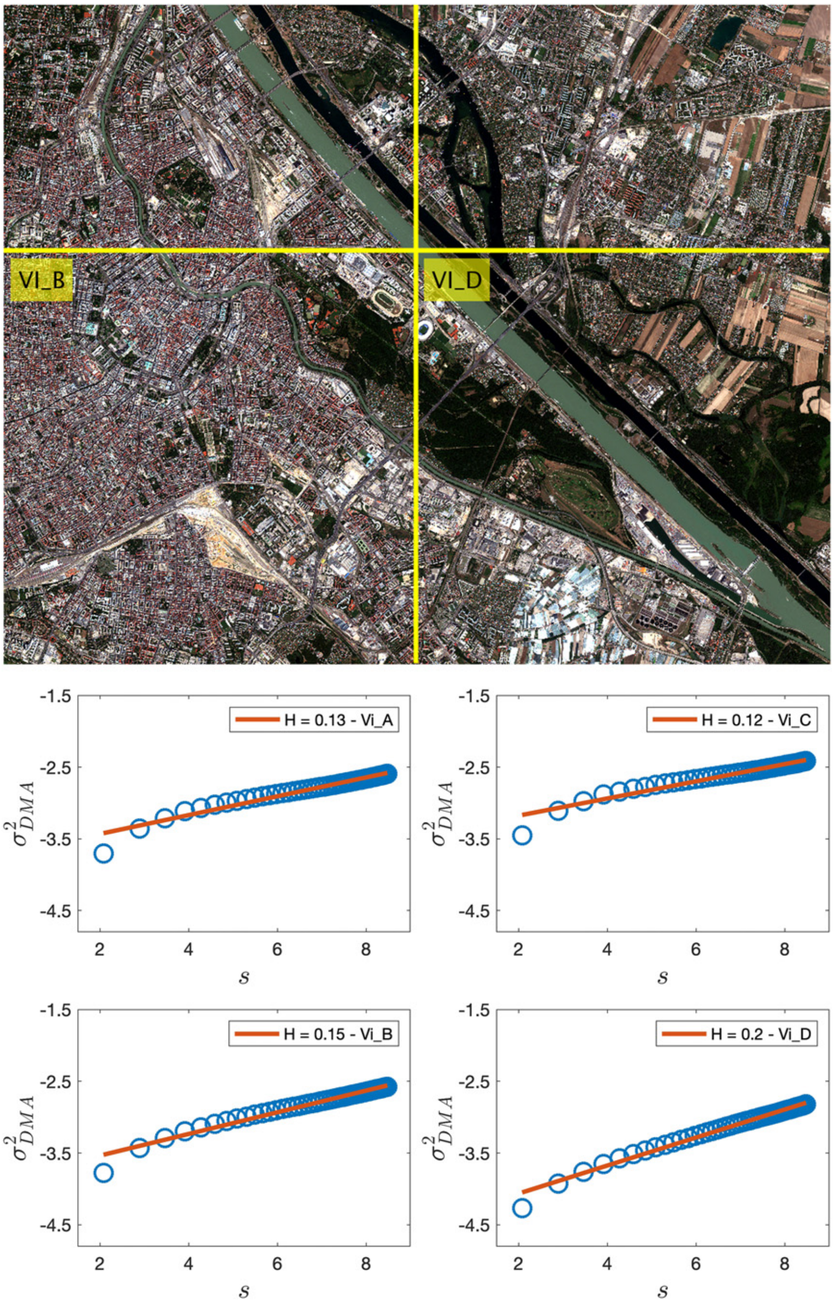

Figure 5. Same as for Fig. 4 but for image N48-181 (Vienna).

3. Data and results

WorldView2 [40] provides panchromatic imagery with 0.46 m resolution and eight-band multispectral imagery with 1.84 m resolution. The subset *European cities* includes WorldView2 images of several European cities and their hinterland, processed by the European Space Imaging GmbH from February 2011 to October 2013 and is referred to as the *Urban Atlas*. With spatial resolutions of the order of 10–30 m, LandSat and Sentinel satellites are very effective at mapping land coverage and cryosphere by identifying spectral signature and broadly classifying areas containing that spectral pattern. Multi-spectral satellite imagery with pixel resolution of the order of 1 m and less provide finer scale features able to investigate Earth crust phenomena at the microscopic level. The high resolution might enable to discriminate fine details of land use/land cover such as farmland, urban areas, quality of road surfaces, and health of plants. The multiple spectral bands yield inter-band spectral information to discriminate texture features [45, 46].

Samples of the analysed urban areas are shown in the top panels of figures 4–7. The images are 1080 × 1080 pixels large. Sub-images, obtained by dividing the main image into four squares of size 540 × 540, are delimited by yellow lines and labelled by A, B, C, D. Here, we report results obtained on the red band. Results obtained

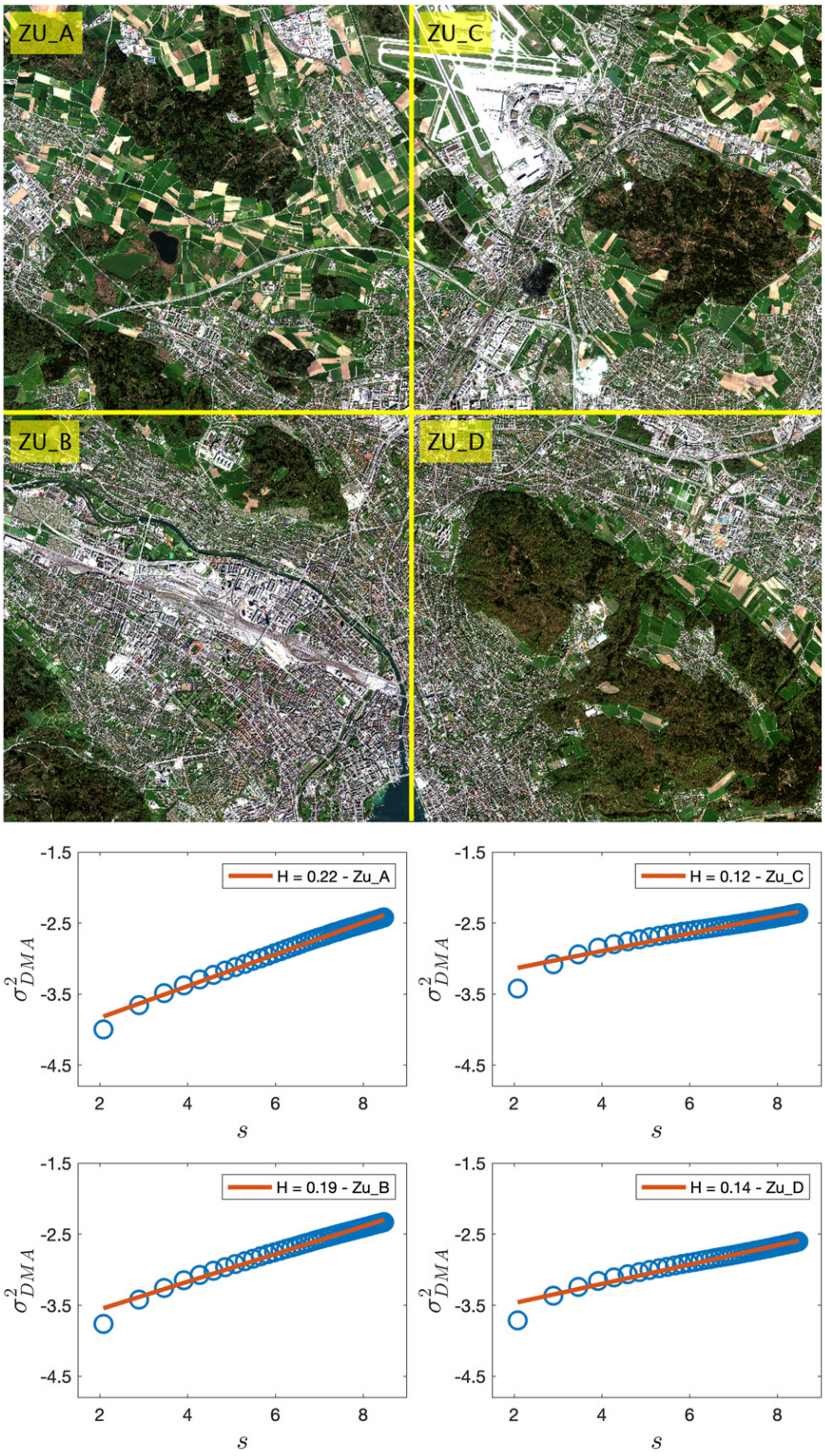

Figure 6. Same as figure 4 but for the image 47-377 (Zurich).

for green and blue bands, different sectors and other cities will be reported in a forthcoming work. Before implementing the DMA algorithm, raw data are converted from the *uint8* to the *double* format. The algorithm is implemented separately on each sub-image, to grasp the variability of the scaling properties of different areas (partially mountainous, suburban and centrally located areas).

Log–log values of σ^2_{DMA} are plotted in the bottom panels of figures 4–7. Deviations from the fully linear trend (expected for an ideal fractal) can be observed particularly at the low scales (small s values) where the σ^2_{DMA} drops down. In order to account for non-ideality extent and the deviations at the extreme scales, multiple computational steps are implemented.

The DMA algorithm has been computed for $n_i \in [2, 49]$, with $i = 1, 2$, which, according to equation (7), results in the s values shown in the horizontal axis of the plots.

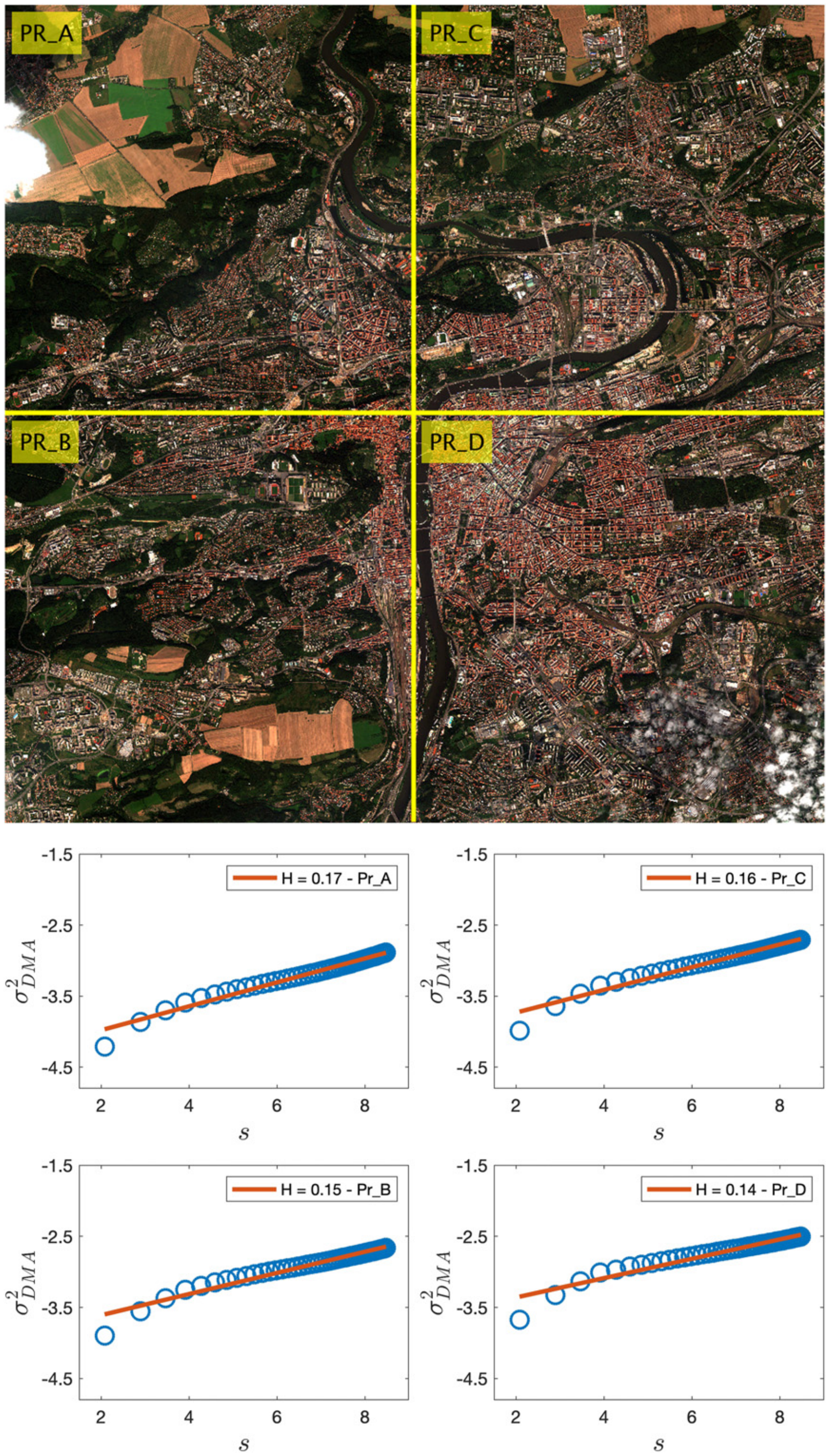

Figure 7. Same as figure 4 but for the image N50-090 (Prague).

Regressions are computed for the first range ($2 < s < 5$), the last range ($5.5 < s < 8.5$) and the whole range of scales, providing three estimates of the Hurst exponent, respectively labelled by H_1, H_2 and H. The values of H_1, H_2 and H are reported for the images shown in figures 4–7, for other images and related subsectors in table 1. The last and the whole range of scales provide quite accurate Hurst exponents (respectively H_2 and H) with excellent goodness of fit as indicated by the high R^2 values in table 1. Higher values of the slope are obtained for the first range of s values (H_1). The origin of the deviation at the low scales reflected in the excess value of H_1 is due to the satellite image resolution mismatch compared to the average size of urban blocks. Being the pixel resolution of the order of 1.84 m, the minimum area detectable by the DMA algorithm is of the order of 1.84 m $\times$ 1.84 m. This area is much smaller than the minimal average urban block area (about 10 m $\times$ 10 m or larger). Thus fewer elementary random built-up components are found at the smallest scales

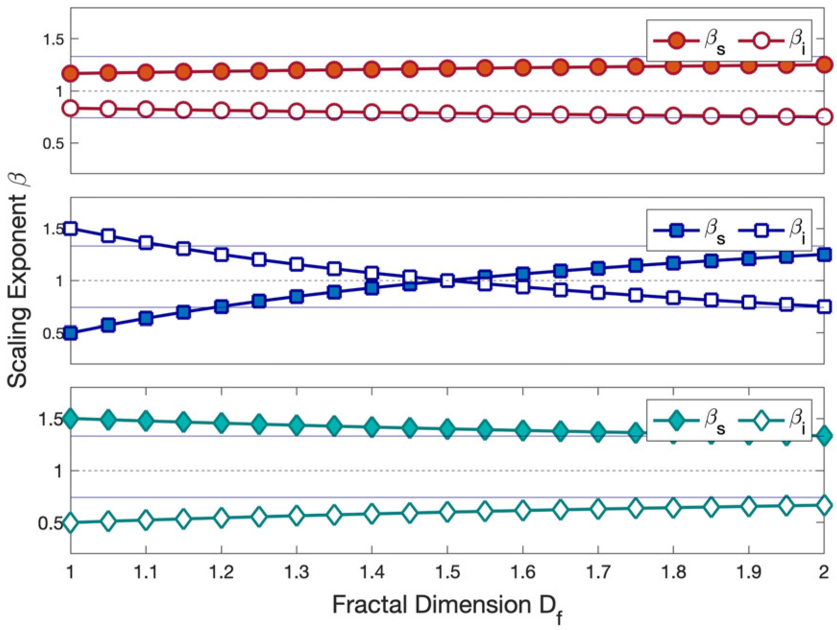

Figure 8. Range of the empirical values for β_i and β_s reported in reference [3] (second column). Analytical expression of the exponents β_i and β_s deduced in references [4–6] (respectively third, fourth and fifth columns). Plot of β_s (filled symbols) and β_i (hollow symbols) as defined by equation (8) (red circle), equation (9) (blue square) and equation (10) (green diamond). A different dependence of the exponents on the fractal dimension is observed: β_s increases (β_i decreases) very slowly with the fractal dimension D_f according to equation (8); a stronger increase (decrease) is found according to equation (9); whereas β_s decreases (β_i increases) with D_f according to equation (10).

compared to the number that would be expected with an ideal self-similar urban structure with block size of the order or smaller than 1.84 m.

Image N45-024 (Turin) is shown in figure 4 (top panel). Log–log results of σ^2_{DMA} are plotted for each sub-image A, B, C, D for the whole range of s scales (bottom panels). The slope is estimated by ordinary linear regression over three different ranges of s values. H_1, H and H_2 corresponding respectively to the first range, full range and last range of s values are reported in table 1. H_2 ranges between $0.10 \div 0.15$, H ranges between $0.12 \div 0.16$, while H_1 ranges between $0.23 \div 0.24$. The Hurst exponent of section D is the highest and indeed corresponds to less urbanised areas (Torino hills). Further results are reported for other Turin areas (image N45-037 and N45-124) in table 1.

Image N48-181 (Vienna) is shown in figure 5 (top panel). The σ^2_{DMA} results are plotted in log–log scale (bottom panels). Sections A, B and C are highly urbanized areas, while section D is less urbanized. This is reflected in the Hurst exponent estimates, which tends to be lower for urbanized areas. H_2 ranges between $0.09 \div 0.17$, H ranges between $0.12 \div 0.20$, while H_1 ranges between $0.22 \div 0.27$ (table 1). Further results are reported for other areas of Vienna (image N48-006 and N48-465) in table 1.

Image N47-377 (Zurich) is shown in figure 6 (top panel). The σ^2_{DMA} results are plotted in log–log scale (bottom panels). The most densely urbanized area looks section B, while the least section A. Overall, the city of Zurich seems more heterogeneous compared to Turin (figure 4) and Vienna (figure 5) with large wooded areas frequently interrupting the urbanized grid. This is reflected in the Hurst exponent, which takes higher and less diversified values than for Torino and Vienna. H_2 ranges between $0.10 \div 0.20$, H ranges between $0.12 \div 0.22$, while H_1 ranges between $0.22 \div 0.28$ (table 1). Further results are reported for other areas of Zurich (images N47-167 and N48-230) in table 1.

The image N50-090 of the city of Prague is shown in figure 7 (top panel) and σ^2_{DMA} results are reported in log–log scale (bottom panels) for each of the four sections of the whole image. H_2 ranges between $0.11 \div 0.16$, H ranges between $0.14 \div 0.17$, while H_1 takes the value 0.26. Further results are reported for other areas of Prague (images N50-045 and N49-908) in table 1.

The fractal dimension D_f can be estimated by using the Hurst exponents estimated above in equation (2). D_f values calculated by introducing the value H_2 in the equation (2) are reported in the last columns of the table 1 for the sectors A, B, C, D of the above described images and other images of the same cities. Similar D_f values can be easily obtained by using H as well.

Table 1. Hurst exponents estimated for the WorldView2 satellite images N45-024, N45-037, N45-124 (Torino); N48-181, N48-006, N48-465 (Vienna); N47-377, N47-230, N47-167 (Zurich); N50-090, N50-045, N49-908 (Prague). The Hurst exponents H_1, H and H_2 have been obtained by implementing the 2*d*-DMA algorithm over the first, whole and last range of *s* values as summarised in section 2. For each image the Hurst exponent is estimated for 4 cross-sections (different urban areas) labelled A, B, C, D as shown in figure 4 for the image N45-024. Last column reports the estimates of the fractal dimension by using $D_f = d - H$ with the Hurst exponents H_2 and $d = 2$. Using the Hurst exponents results in the second column, referred to as H, alternative but similar values of D_f can be obtained.

Image	Section	H_1	H	H_2	R^2	D_f
			Torino			
ID: N45-024	A	0.23	0.12	0.10	0.93	1.90
X: 45.024	B	0.23	0.13	0.11	0.95	1.89
Y: 7.709	C	0.24	0.13	0.11	0.94	1.89
D: 09-2011	D	0.25	0.16	0.15	0.97	1.85
ID: N45-037	A	0.31	0.30	0.32	1.00	1.68
X coord: 45.037	B	0.27	0.25	0.27	0.99	1.73
Y coord: 7.189	C	0.28	0.23	0.23	0.99	1.77
Date: 09-2011	D	0.33	0.30	0.31	1.00	1.69
ID: N45-124	A	0.30	0.28	0.30	1.00	1.70
X coord: 45.125	B	0.27	0.22	0.23	0.99	1.77
Y coord: 7.303	C	0.25	0.16	0.13	0.97	1.87
Date: 09-2011	D	0.26	0.17	0.15	0.98	1.85
			Vienna			
ID: N48-181	A	0.23	0.13	0.11	0.94	1.89
X: 48.181	B	0.24	0.15	0.13	0.97	1.87
Y: 16.448	C	0.22	0.12	0.09	0.93	1.90
D: 07-2012	D	0.27	0.20	0.17	0.98	1.83
ID: N48-006	A	0.33	0.26	0.23	0.99	1.77
X: 48.006	B	0.38	0.30	0.27	0.99	1.73
Y: 16.446	C	0.33	0.29	0.27	1.00	1.73
D: 07-2012	D	0.33	0.26	0.22	0.99	1.78
ID: N48-465	A	0.41	0.30	0.27	0.99	1.73
X: 48.466	B	0.39	0.32	0.31	1.00	1.69
Y: 16.619	C	0.40	0.29	0.26	0.99	1.74
D: 07-2012	D	0.40	0.28	0.24	0.98	1.76
			Zurich			
ID: N47-377	A	0.28	0.22	0.20	0.99	1.80
X: 47.37	B	0.27	0.19	0.17	0.98	1.83
Y: 8.500	C	0.23	0.12	0.10	0.93	1.90
D: 04-2014	D	0.22	0.14	0.12	0.96	1.88
ID: N47-167	A	0.26	0.19	0.16	0.98	1.84
X: 47.167	B	0.27	0.20	0.19	0.99	1.81
Y: 8.702	C	0.28	0.23	0.23	0.99	1.77
Date: 07-2010	D	0.26	0.18	0.16	0.98	1.84
ID: N47-230	A	0.28	0.23	0.21	0.99	1.79
X: 47.230	B	0.27	0.21	0.19	0.99	1.81
Y: 8.501	C	0.29	0.23	0.21	0.99	1.79
D: 04-2014	D	0.27	0.21	0.18	0.99	1.82
			Prague			
ID: N50-090	A	0.26	0.17	0.16	0.97	1.84
X: 50.091	B	0.26	0.15	0.12	0.95	1.88
Y: 14.371	C	0.26	0.16	0.14	0.96	1.86
D: 08-2013	D	0.26	0.14	0.11	0.93	1.89
ID: N50-045	A	0.25	0.18	0.17	0.99	1.83
X: 50.046	B	0.24	0.14	0.12	0.95	1.88
Y: 14.313	C	0.25	0.19	0.19	0.99	1.81
D: 03-2012	D	0.26	0.21	0.21	0.99	1.79
ID: N49-908	A	0.29	0.24	0.24	0.99	1.76
X: 49.909	B	0.34	0.32	0.32	1.00	1.68
Y: 15.273	C	0.36	0.32	0.33	1.00	1.67
D: 07-2013	D	0.33	0.29	0.30	1.00	1.70

Table 2. Scaling exponents β_i and β_s obtained by using the values of D_f reported in table 1. The values for the sections A, B, C, D are obtained by using equation (8) and equation (9) with $\gamma = 1.5$ and equation (10), with $D_p = D_f + 1$.

Reference		[4]				[5]				[6]			
		A	B	C	D	A	B	C	D	A	B	C	D
						Vienna							
N48-181	β_i	0.76	0.76	0.76	0.76	0.80	0.81	0.80	0.83	0.65	0.65	0.65	0.64
	β_s	1.24	1.24	1.24	1.24	1.20	1.20	1.20	1.17	1.35	1.35	1.35	1.36
N48-006	β_i	0.76	0.77	0.77	0.76	0.85	0.87	0.87	0.84	0.64	0.63	0.63	0.64
	β_s	1.23	1.23	1.23	1.23	1.15	1.13	1.13	1.16	1.36	1.37	1.37	1.36
N48-465	β_i	0.77	0.77	0.77	0.77	0.87	0.89	0.86	0.85	0.63	0.63	0.63	0.64
	β_s	1.23	1.23	1.23	1.23	1.13	1.11	1.14	1.15	1.37	1.37	1.36	1.36
						Prague							
N50-090	β_i	0.76	0.76	0.76	0.76	0.82	0.81	0.81	0.80	0.65	0.65	0.65	0.65
	β_s	1.24	1.24	1.24	1.24	1.18	1.19	1.18	1.19	1.35	1.35	1.35	1.35
N50-045	β_i	0.76	0.76	0.76	0.76	0.82	0.80	0.83	0.84	0.65	0.65	0.64	0.64
	β_s	1.24	1.24	1.24	1.24	1.18	1.20	1.17	1.16	1.35	1.35	1.36	1.36
N50-908	β_i	0.77	0.77	0.77	0.77	0.85	0.89	0.89	0.88	0.64	0.63	0.62	0.63
	β_s	1.23	1.23	1.23	1.23	1.15	1.11	1.10	1.12	1.36	1.37	1.37	1.37
						Torino							
N45-024	β_i	0.76	0.76	0.76	0.76	0.79	0.79	0.79	0.81	0.65	0.65	0.65	0.65
	β_s	1.24	1.24	1.24	1.24	1.21	1.21	1.21	1.19	1.34	1.35	1.35	1.35
N45-037	β_i	0.77	0.77	0.76	0.77	0.89	0.87	0.85	0.89	0.63	0.63	0.64	0.63
	β_s	1.23	1.23	1.23	1.23	1.11	1.13	1.15	1.11	1.37	1.37	1.36	1.37
N45-124	β_i	0.77	0.76	0.76	0.76	0.88	0.85	0.80	0.81	0.63	0.64	0.65	0.65
	β_s	1.23	1.23	1.24	1.24	1.12	1.15	1.20	1.19	1.37	1.36	1.35	1.35
						Zurich							
N47-377	β_i	0.76	0.76	0.76	0.76	0.83	0.82	0.79	0.80	0.64	0.65	0.65	0.65
	β_s	1.24	1.24	1.24	1.24	1.17	1.18	1.21	1.20	1.36	1.35	1.34	1.35
N47-167	β_i	0.76	0.76	0.76	0.76	0.81	0.83	0.85	0.81	0.65	0.64	0.64	0.65
	β_s	1.24	1.24	1.23	1.24	1.18	1.17	1.15	1.18	1.35	1.36	1.36	1.35
N47-230	β_i	0.76	0.76	0.76	0.76	0.84	0.83	0.84	0.82	0.64	0.64	0.64	0.64
	β_s	1.24	1.24	1.24	1.24	1.16	1.17	1.16	1.18	1.36	1.36	1.36	1.35

4. Discussion

The values of the Hurst exponent H and fractal dimension D_f summarized in table 1 will be compared with those reported in previous works [10–17, 19, 20] in this section. Next, the exponent β of the scaling law $Y \sim N^{\beta}$ will be estimated by introducing the values of D_f into the relationships worked out in [4–6].

As mentioned in the introduction, the fractal dimension D_f has been estimated on cities by approaches as diverse as box-counting, radial method isarithm and variogram. The Hurst exponent takes a unique value hence allowing the comparison and linking results obtained by methods implemented over different embedding dimensions d. Depending on the embedding Euclidean dimension $d = 1$, $d = 2$ and $d = 3$ of the fractal set and using the equation (2), $D_f = d - H$ takes values respectively in the range $(0 \div 1.0)$, $(1.0 \div 2.0)$ and $(2.0 \div 3.0)$.

Values of the fractal dimension $D_f < 1$ have been obtained in suburban fragmented areas when one-dimensional fractal measures (e.g. the radial method) are adopted [17]. To understand how such $D_f < 1$ values emerge, one can think of the well-known Cantor set, a fractal obtained by repeatedly removing parts of a line segments. Thus a fractal set with $0 < D_f < 1$ resembles a fragmented structure between a point ($D_f = 0$) and a line ($D_f = 1$).

Fractal dimensions ranging between $1.28 \leqslant D_f \leqslant 1.70$ have been reported for Omaha and New York city in [12], between $1.44 \leqslant D_f \leqslant 1.62$, and $1.68 \leqslant D_f \leqslant 1.50$, for Belgium's 18 largest cities in [13]. Values in the range $1 \leqslant D_f < 1.26$, for dispersed areas, $1.26 \leqslant D_f < 1.54$ for new seeds of urbanised areas, $1.54 \leqslant D_f \leqslant 2$ for densely urbanized and consolidated areas are reported for Lisbon in reference [14]. Several mega-cities and mining cities of China are investigated over different periods: the fractal dimension ranges between $1.57 \leqslant D_f \leqslant 1.74$ in 1990, and $1.57 \leqslant D_f \leqslant 1.78$ in 2000 [15] and between $1.62 \leqslant D_f \leqslant 1.80$ [16].

The fractal dimensions of built-up surfaces in central and peripheral parts of 40 European urban agglomerations using satellite images of the CORINE land cover database has been analysed in [17]. The fractal measure

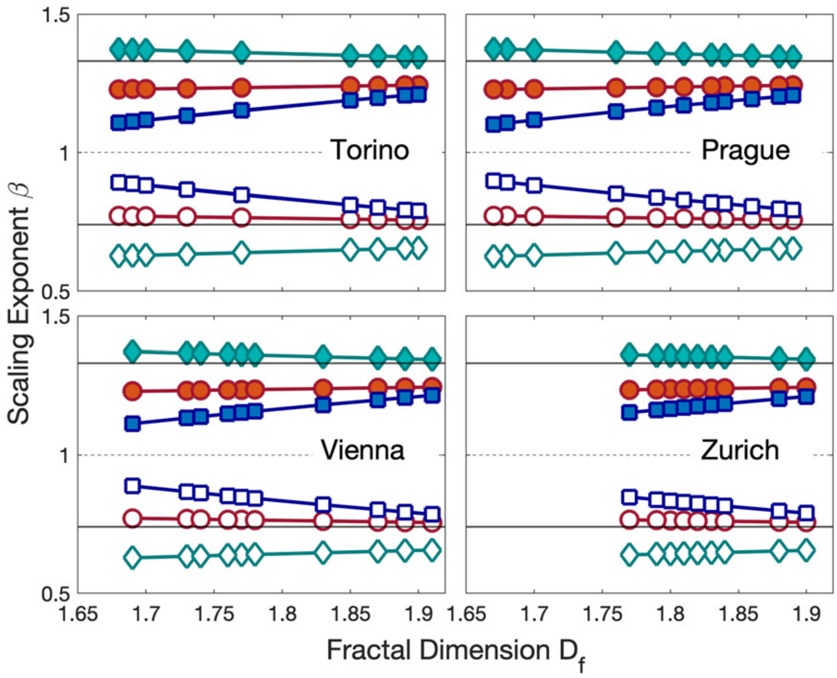

Figure 9. Experimental exponents β_s (filled symbols) and β_i (hollow symbols) as defined by equation (8) (circle), equation (9) (square) and equation (10) (diamond) for different areas of Torino, Zurich, Vienna and Prague. A different dependence of the exponents on the fractal dimension is observed.

is implemented on the radial distribution density $D(r)$ and cumulative population functions $P(r)$ with the variable r defined in a one-dimensional Euclidean dimension with $d = 1$, which for a fragmented urban structure (detached suburban areas) provide fractal dimension lower than 1 in most of the cases.

Fractal dimensions of satellite images of cities are obtained by (i) isarithm, (ii) triangular prism and (iii) variogram ranging respectively between (i) $2.80 \leqslant D_f \leqslant 3.00$; (ii) $2.60 \leqslant D_f \leqslant 2.80$, for urban, forest and grass, $2.30 \leqslant D_f \leqslant 2.80$ for cropland and pasture; $2.20 \leqslant D_f \leqslant 2.60$ for water; (iii) $2.80 \leqslant D_f \leqslant 3.00$ for cropland and water; $D_f \geqslant 3.00$ for urban, forest and grass [19]. The triangular prism yields lower values of D_f compared to those obtained by isarithm and variogram methods. The images analysed by triangular prism date back to 1975, while the other images were acquired in 2000 (isarithm and variogram). After 25 years, the city had become a large metropolis where manmade infrastructure with roads, highways, and buildings filled the area. Such changes in the urban landscape can reasonably explain the increased value of D_f and the corresponding decrease of H. The fractal dimension of red band satellite images of the Indianapolis area ranges respectively between $2.72 \leqslant D_f \leqslant 2.82$ (isarithm), $2.78 \leqslant D_f \leqslant 2.93$ (triangular prism), and $2.88 \leqslant D_f \leqslant 2.96$ (variogram) [20]. On average the H values obtained by using satellite images are smaller than those obtained by using traditional data sets as cartographic maps.

To further substantiate our study, the values of the Hurst exponent H and of the fractal dimension D_f of satellite images as those in figures 4–7 will be validated against the relationships linking β and D_f deduced in references [4–6] which are briefly recalled below.

Under the assumption of incremental network growth and bounded human effort, infrastructural and socio-economic features are written as power laws of the population size $Y \sim N^{\beta}$ respectively with exponents [4]:

$$\beta_i = 1 - \frac{D_f}{d(d + D_f)} \qquad \beta_s = 1 + \frac{D_f}{d(d + D_f)}. \tag{8}$$

In reference [5], the interaction strength between individuals is modelled in terms of a scalar field varying inversely with the distance. Based on this assumption, the total interaction intensity is obtained in the form of a power law of the population size, for the infrastructural and socio-economic quantities with scaling exponents respectively:

$$\beta_i = \frac{\gamma}{D_f} \qquad \beta_s = 2 - \frac{\gamma}{D_f}, \tag{9}$$

with γ varying in the range $1.0 \div 1.5$ (noteworthy $\gamma = 1.0$ corresponds to the Newtonian gravitational law in $d = 2$). The long-range interaction regime, with $\gamma/D_f < 1$ and $\beta_s > 1$, implies that superlinear socio-economic scaling behaviour occurs when each individual can interact with all other individuals of the city.

In reference [6] socio-economic interactions are assumed to occur in a three dimensional fractal cloud rather than on the two-dimensional fractal infrastructure generated by the urban plan. According to this work, since buildings extend into the third dimension, the population is distributed as a fractal in space, with dimension D_p, where $D_f \leqslant D_p \leqslant D_f + 1$. Under this assumption, the authors write the scaling exponents for the infrastructures and the socio-economic activities as:

$$\beta_i = \frac{D_f}{D_p} \qquad \beta_s = 2 - \frac{D_f}{D_p}. \tag{10}$$

For the convenience of the discussion, the scaling exponents are plotted as a function of the fractal dimension D_f in the bottom panel of figure 8. The empirical values of β_i and β_s reported in [3] and the relationships (8)–(10) are given for the ease of comparison respectively in the second, third, fourth and fifth column of the table in the top panel of figure 8.

One can note that the exponents β_i and β_s deduced in references [4–6] exhibit a different dependence on D_f. In particular, the exponent β_s increases very slowly with the fractal dimension D_f according to equation (8). A steeper increase of β_s is found according to the equation (9). Surprisingly, β_s decreases with D_f according to equation (10) and reference [6]. Analogously, one can note that β_i decreases according to equations (8) and (9), whereas β_i increases according to equation (10).

A few peculiar properties of the scaling law exponents deserve to be further outlined. The model [5] exhibits a quite interesting physically sound behaviour. At the value $D_f = 1.5$, β_i and β_s become respectively larger and smaller than 1. One can bear in mind that a fractal dimension ($1.0 < D_f < 1.5$) would correspond to a urban area distributed mostly along a line (i.e. more similar to a one-dimensional geometrical structure), whereas a fractal dimension ($1.5 < D_f < 2.0$) would correspond to a urban area distributed almost over a square (i.e. more similar to a two-dimensional geometrical structure). The inversion of the values of the exponents can be related to the different constraints posed by a urban area mostly distributed along a line, with fractal dimension $D_f \to 1$. Such urban topology would clearly imply that the cost of the physical infrastructure exceeds over the socio-economic advantage of the urban organization. Conversely, $D_f \to 2$ corresponds to a more compact urban structure almost regularly distributed over a two-dimensional surface, where the costs of the physical infrastructure are much better compensated by the socio-economic organization advantage. As a final comment, we note that in the case of [6], the behaviour of $beta_s$ does not exhibit the increasing dependence on D_f that would be expected on account of other studies and experiments and that seems to be grounded on physically sound arguments related to the benefits of the urban organization.

The different behaviour of the scaling exponents provided by the models [4–6] is further discussed in terms of the derivatives with respect to D_f. Consider for example the derivative of β_s (the derivative $\partial\beta_i/\partial D_f$ yield similar expressions but with opposite sign). The calculation yields respectively for equation (8) (reference [4]):

$$\partial\beta_s/\partial D_f = 1/(d + D_f)^2, \tag{11}$$

for equation (9) (reference [5]):

$$\partial\beta_s/\partial D_f = \gamma/D_f^2, \tag{12}$$

for equation (10) (reference [6]):

$$\partial\beta_s/\partial D_f = -1/(1 + D_f)^2 \quad \text{if } D_p = D_f + 1$$

otherwise

$$\partial\beta_s/\partial D_f = -1/D_f^2 \quad \text{if } D_p = D_f. \tag{13}$$

The derivatives of the exponents β_s exhibit a different dependence on D_f, hence confirming the behaviour shown by the curves in figure 8.

The fractal dimension values (ranging between $1.6 \leqslant D_f \leqslant 1.8$ and $1 < D_f < 2$) used for the scaling law estimates were taken from third party sources in [4–6]. In this work, the exponents β_i and β_s are calculated by introducing the values of D_f (table 1) into the equations (8)–(10). Values are shown in table 2. Columns from 3 to 6 show the values obtained by equation (8); equation (9) with $\gamma = 1.5$ correspond to columns from 7 to 10; equation (10) with $D_p = D_f + 1$ correspond to columns from 11 to 14. The analysed areas have infrastructures scaling sub-linearly and socio-economic interactions scaling super-linearly with exponents in the range of empirical values according to reference [3] when equations (8) and (9) are used. The values of the exponent yielded by equation (10) systematically exceed the expected values. The values are plotted in figure 9, where the range of empirical values (column 2 of the table in figure 8) are also indicated by thin horizontal lines.

5. Conclusions

This work enriches the existing literature on two fronts. First, it provides a new method for urban classification capable of distinguishing different areas such as urban and suburban areas. In particular, the Hurst exponent H (resp., the fractal dimension D_f) is smaller (larger) for highly urbanized areas and larger (smaller) for detached rural areas. The Hurst exponent H of several large European cities has been estimated by implementing the DMA algorithm on high resolution remotely sensed images (WorldView2 Urban Atlas database). The values of H are linked to the fractal dimension D_f through the relationship (2). Our estimates provide $0.10 \leqslant H \leqslant 0.30$ for the Hurst exponent, which correspond to fractal dimensions ranging between $1.65 \leqslant D_f \leqslant 1.90$. Interestingly, we obtain slightly smaller Hurst exponent and higher fractal dimension on average with respect to the estimates of the urban fractal dimensions reported in [12–15]. Our values of the Hurst exponent are closer to those provided in references [16, 19, 20]. This result seems to suggest that highly reproducible values are obtained when satellite images are used as opposed to those provided by other data sets.

Second, the manuscript demonstrates that a geometrical approach to urban scaling theory, which exploit the statistical structure of high resolution satellite images of cities, provides robust estimates and validation of urban scaling laws. A rich theory has developed a number of models that describe the characteristic power law behaviour of features exhibiting super-linear or sub-linear scaling respectively for socio-economic and infrastructural variables. Interestingly, for the quantification of such formulae, the theoretical framework relies on fractal measures. By using the definitions of the scaling exponents reported in the table at the top of figure 8, β_i and β_s can be calculated. The results for the images N45-024, N48-181, N47-377 and N50-090 of the cities of Turin, Vienna, Zurich and Prague are reported in table 2 and plotted in figure 9. The outcomes are physically sound and could help to reconcile controversial perspectives to the ultimate purpose to achieve a shared knowledge infrastructure for urban landscape analysis of broad interest. Thus, the proposed method can be used alone or in combination with other measures and approaches to provide significant new insights in urban scaling model analysis and in designing the related needs for intervention and policy-making activities.

Acknowledgments

This work received financial support from the FuturICT2.0 project (a FLAG-ERA Initiative within the Joint Transnational Calls 2016, Grant No. JTC-2016-004) and from the SIP project (Italian Ministry of Economic Development (MISE) Programme on 'Emerging Technologies in the context of 5G').

Data availability statement

The data that support the findings of this study are openly available.

ORCID iDs

Anna Carbone https://orcid.org/0000-0003-4945-9165
Pietro Murialdo https://orcid.org/0000-0003-4967-5095
Carina Toxqui-Quitl https://orcid.org/0000-0003-1728-8138

References

[1] Gao J, Zhang Y-C and Zhou T 2019 Computational socioeconomics *Phys. Rep.* **817** 1–104
[2] Carbone A, Jensen M and Sato A-H 2016 Challenges in data science: a complex systems perspective *Chaos Solitons Fractals* **90** 1–7
[3] Bettencourt L M A, Lobo J, Helbing D, Kühnert C and West G B 2007 Growth, innovation, scaling, and the pace of life in cities *Proc. Natl Acad. Sci. USA* **104** 7301–6
[4] Bettencourt L M A 2013 The origins of scaling in cities *Science* **340** 1438–41
[5] Ribeiro F L, Meirelles J, Ferreira F F and Neto C R 2017 A model of urban scaling laws based on distance dependent interactions *R. Soc. Open Sci.* **4** 160926
[6] Molinero C and Thurner S 2021 How the geometry of cities determines urban scaling laws *J. R. Soc. Interface* **18** 20200705
[7] Portugali J 2012 *Self-Organization and the City* (Springer)
[8] Haken H and Portugali J 2021 Urban scaling, urban regulatory focus and their interrelations *Synergetic Cities: Information, Steady State and Phase Transition: Implications to Urban Scaling, Smart Cities and Planning* pp 199–215
[9] Mandelbrot B B 1977 *Fractals: Form, Chance and Dimension* (San Francisco, CA: Freeman)
[10] Batty M and Longley P A 1987 Fractal-based description of urban form *Environ. Plan.* B **14** 123–34
[11] Frankhauser P 1998 The fractal approach. A new tool for the spatial analysis of urban agglomerations *Population: An English Selection* (Paris, France) pp 205–40
[12] Shen G 2002 Fractal dimension and fractal growth of urbanized areas *Int. J. Geogr. Inf. Sci.* **16** 419–37

[13] Tannier C and Thomas I 2013 Defining and characterizing urban boundaries: a fractal analysis of theoretical cities and Belgian cities *Comput. Environ. Urban Syst.* **41** 234–48

[14] Encarnação S, Gaudiano M, Santos F C, Tenedório J A and Pacheco J M 2012 Fractal cartography of urban areas *Sci. Rep.* **2** 1–5

[15] Chen Y 2013 A set of formulae on fractal dimension relations and its application to urban form *Chaos Solitons Fractals* **54** 150–8

[16] Emerson C W, Lam N S N and Quattrochi D A 2005 A comparison of local variance, fractal dimension, and Moran's I as aids to multispectral image classification *Int. J. Remote Sens.* **26** 1575–88

[17] Guérois M and Pumain D 2008 Built-up encroachment and the urban field: a comparison of forty European cities *Environ. Plan.* A **40 9** 2186–203

[18] Lemoy R and Caruso G 2021 Radial analysis and scaling of urban land use *Sci. Rep.* **11** 1–8

[19] Liang B, Weng Q and Tong X 2013 An evaluation of fractal characteristics of urban landscape in Indianapolis, USA, using multi-sensor satellite images *Int. J. Remote Sens.* **34** 804–23

[20] Liang B and Weng Q 2018 Characterizing urban landscape by using fractal-based texture information *Photogramm. Eng. Remote Sens.* **84** 695–710

[21] Rozenfeld H D, Rybski D, Gabaix X and Makse H A 2011 The area and population of cities: new insights from a different perspective on cities *Am. Econ. Rev.* **101** 2205–25

[22] Levinson D 2012 Network structure and city size *PLoS One* **7** e29721

[23] Yakubo K, Saijo Y and Korošak D 2014 Superlinear and sublinear urban scaling in geographical networks modeling cities *Phys. Rev.* E **90** 022803

[24] Wu H, Levinson D and Sarkar S 2019 How transit scaling shapes cities *Nat. Sustain.* **2** 1142–8

[25] Keuschnigg M, Mutgan S and Hedström P 2019 Urban scaling and the regional divide *Sci. Adv.* **5** eaav0042

[26] Dong L, Huang Z, Zhang J and Liu Y 2020 Understanding the mesoscopic scaling patterns within cities *Sci. Rep.* **10** 1–11

[27] Altmann E G 2020 Spatial interactions in urban scaling laws *PLos One* **15** e0243390

[28] Cottineau C, Hatna E, Arcaute E and Batty M 2017 Diverse cities or the systematic paradox of urban scaling laws *Comput. Environ. Urban Syst.* **63** 80–94

[29] Arcaute E, Hatna E, Ferguson P, Youn H, Johansson A and Batty M 2015 Constructing cities, deconstructing scaling laws *J. R. Soc. Interface* **12** 20140745

[30] Rybski D, Arcaute E and Batty M 2019 Urban scaling laws *Environ. Plan. B* **46** 1605–10

[31] Elvidge C D, Baugh K E, Kihn E A, Kroehl H W, Davis E R and Davis C W 1997 Relation between satellite observed visible-near infrared emissions, population, economic activity and electric power consumption *Int. J. Remote Sens.* **18** 1373–9

[32] Ebener S, Murray C, Tandon A and Elvidge C C 2005 From wealth to health: modelling the distribution of income per capita at the sub-national level using night-time light imagery *Int. J. Health Geogr.* **4** 1–17

[33] Donaldson D and Storeygard A 2016 The view from above: applications of satellite data in economics *J. Econ. Perspect.* **30** 171–98

[34] Jean N, Burke M, Xie M, Davis W M, Lobell D B and Ermon S 2016 Combining satellite imagery and machine learning to predict poverty *Science* **353** 790–4

[35] Wellmann T *et al* 2020 Remote sensing in urban planning: contributions towards ecologically sound policies? *Landscape Urban Plan.* **204** 103921

[36] Burke M, Driscoll A, Lobell D B and Ermon S 2021 Using satellite imagery to understand and promote sustainable development *Science* **371** eabe8628

[37] Isichenko M B 1992 Percolation, statistical topography, and transport in random media *Rev. Mod. Phys.* **64** 961

[38] Hristopulos D T 2020 *Random Fields for Spatial Data Modeling* (Netherlands: Springer)

[39] Carbone A 2007 Algorithm to estimate the Hurst exponent of high-dimensional fractals *Phys. Rev.* E **76** 056703

[40] Urban Atlas 2021 The ESA third party mission collection of the largest European urban areas recorded by the WorldView-2 satellite https://tpm-ds.eo.esa.int/oads/access/collection/WorldView-2

[41] FRACLAB 2021 We use the CLF algorithm included in the package FRACLAB downloadable at https://project.inria.fr/fraclab/

[42] Carbone A, Chiaia B M, Frigo B and Türk C 2010 Snow metamorphism: a fractal approach *Phys. Rev.* E **82** 036103

[43] Türk C, Carbone A and Chiaia B M 2010 Fractal heterogeneous media *Phys. Rev.* E **81** 026706

[44] Valdiviezo-N J C, Castro R, Cristóbal G and Carbone A 2014 Hurst exponent for fractal characterization of LANDSAT images *Remote Sensing and Modeling of Ecosystems for Sustainability XI* vol 9221 (USA: International Society for Optics and Photonics) p 922103

[45] Arreola-Esquivel M, Toxqui-Quitl C, Delgadillo-Herrera M, Padilla-Vivanco A, Ortega-Mendoza G and Carbone A 2021 Non-binary snow index for multi-component surfaces *Remote Sens.* **13** 2777

[46] Safia A and He D-C 2015 Multiband compact texture unit descriptor for intra-band and inter-band texture analysis *ISPRS J. Photogramm. Remote Sens.* **105** 169–85